ASME Journal of Mechanical Design
Online journal at:
https://asmedigitalcollection.asme.org/mechanicaldesign

Bin Zhou
School of Mechanical Engineering;
Intelligent Interconnected Systems Laboratory of
Anhui Province,
Hefei University of Technology,
193 Tunxi Road,
Hefei 230009, China
e-mail: zhoubin13865923505@163.com

Sipan Li[1]
School of Mechanical Engineering,
Hefei University of Technology,
193 Tunxi Road,
Hefei 230009, China
e-mail: zb13865923505@163.com

Bin Zi
School of Mechanical Engineering,
Hefei University of Technology,
193 Tunxi Road,
Hefei 230009, China
e-mail: hfutzibin888@163.com

Bing Chen
School of Mechanical Engineering,
Hefei University of Technology,
193 Tunxi Road,
Hefei 230009, China
e-mail: chbing@hfut.edu.cn

Weidong Zhu
Department of Mechanical Engineering,
University of Maryland, Baltimore County,
1000 Hilltop Circle,
Baltimore, MD 21250
e-mail: wzhu@umbc.edu

Multi-Objective Optimal Design of a Cable-Driven Parallel Robot Based on an Adaptive Adjustment Inertia Weight Particle Swarm Optimization Algorithm

Cable-driven parallel robots (CDPRs) have been widely used in engineering fields because of their significant advantages including high load-bearing capacity, large workspace, and low inertia. However, the impact of convergence speed and solution accuracy of optimization approaches on optimal performances can become a key issue when it comes to the optimal design of CDPR applied to large storage space. An adaptive adjustment inertia weight particle swarm optimization (AAIWPSO) algorithm is proposed for the multi-objective optimal design of CDPR. The kinematic and static models of CDPR are established based on the principle of virtual work. Subsequently, two performance indices including workspace and dexterity are derived. A multi-objective optimization model is established based on performance indices. The AAIWPSO algorithm introduces an adaptive adjustment inertia weight to improve the convergence efficiency and accuracy of traditional particle swarm optimization (PSO) algorithm. Numerical examples demonstrate that final convergence values of the objective function by the AAIWPSO algorithm can almost be 14~20% and 19~40% higher than those by the PSO algorithm and genetic algorithm (GA) for the optimal design of CDPR with different configurations and masses of end-effectors, respectively. [DOI: 10.1115/1.4062458]

Keywords: cable-driven parallel robots, multi-objective optimal design, performance index, adaptive adjustment inertia weight, PSO algorithm, genetic algorithm

1 Introduction

Cable-driven parallel robots (CDPRs) are known as a type of mechanical structure that is actuated by cables instead of rigid links [1,2]. Parallel cables are widely used in CDPRs to provide constraints to realize multiple degrees-of-freedom. Owing to these advantages of small inertia [3] and a big ratio of the load to the weight of the cable-driven mechanism [4], CDPRs have many good system performances [5]. In addition, because of the significant features of large workspace, modular reconfigurability [6], and superior flexibility [7], CDPRs have been widely used in many fields such as construction [8], rehabilitation [9], telescope [10], and 3D printing [11]. However, performances of CDPRs need to be optimized when it comes to the effect of inherent characteristics on motion accuracy and efficiency.

One of the typical types of CDPRs is that cables provide tensions for end-effectors, which enables end-effectors to realize movements in a certain space [12]. Based on this mechanical characteristic of CDPRs, there are many factors, including geometric parameters [13], modular configurations [14], and tensions of cables [15], which can affect system performances. Gao et al. [16] proposed a novel tension distribution algorithm for cable-driven parallel robots, and the algorithm can calculate the tension feasible region and efficiently optimize the tension distribution. Based on driving force transmission indexes and geometrical constraints, Zhang et al. [17] constituted multi-objective functions to effectively optimize the singularity, power, interference, and motion range of the parallel mechanism for hip rehabilitation. Gueners et al. [18] studied stiffness optimization of a cable-driven parallel robot for additive manufacturing. Sun et al. [19] proposed a new type of

[1]Corresponding author.

Contributed by the Mechanisms and Robotics Committee of ASME for publication in the Journal of Mechanical Design. Manuscript received November 18, 2022; final manuscript received April 26, 2023; published online May 22, 2023. Assoc. Editor: Leila Notash.

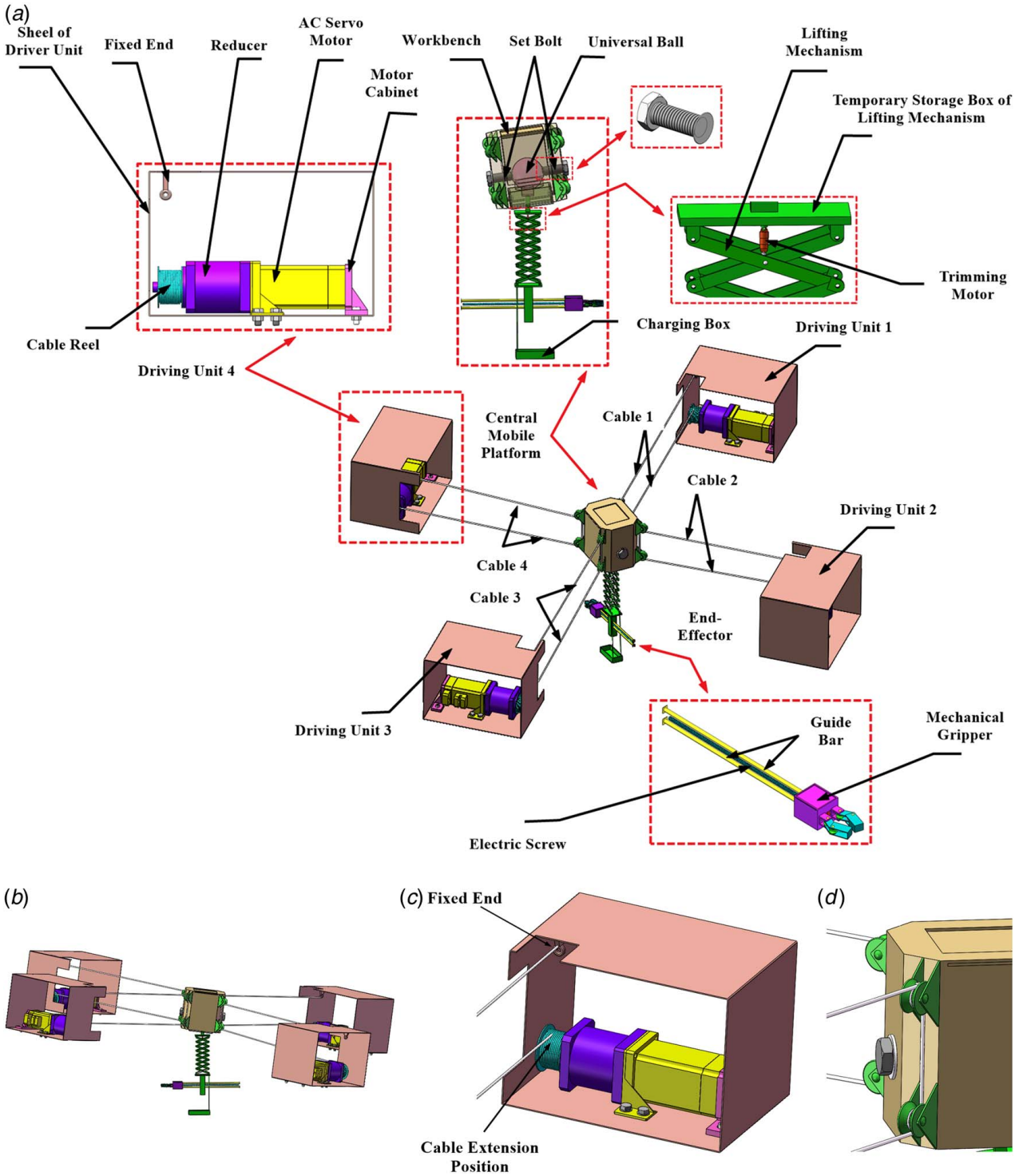

Fig. 1 Mechanical prototype of the CDPR

adaptive CDPR that could passively modify the attachment points on end-effectors, which could effectively increase the rotation workspace without increasing any redundancy.

The above-mentioned research studies mainly focus on configurations and ontology characteristics of CDPRs; however, there are more factors that can influence the degree of improvement in system performances, especially computational efficiency, and accuracy of multi-objective optimization algorithms. If the optimization only comes to mechanism configuration and characteristics of CDPRs, it cannot gain desired results. Thus, the optimization of system performances of CDPRs has great significance for improving the motion accuracy and working efficiency of end-effectors. There are many performance indices that reflect system performances, including sensitivity [20,21], workspace [22,23], kinematic uncertainty [24–26], and dynamic reliability [27,28]. Up to now, there are many optimization algorithms to solve these problems [29,30], such as the genetic algorithm [31], searching algorithm for global optimization [32], and adaptive double-loop kriging algorithm [27]. Based on a newly defined concept of equivalent transmission wrench screws and the genetic algorithm, Meng et al. [33] proposed a modified output transmission index for a high-speed parallel robot with articulated platforms.

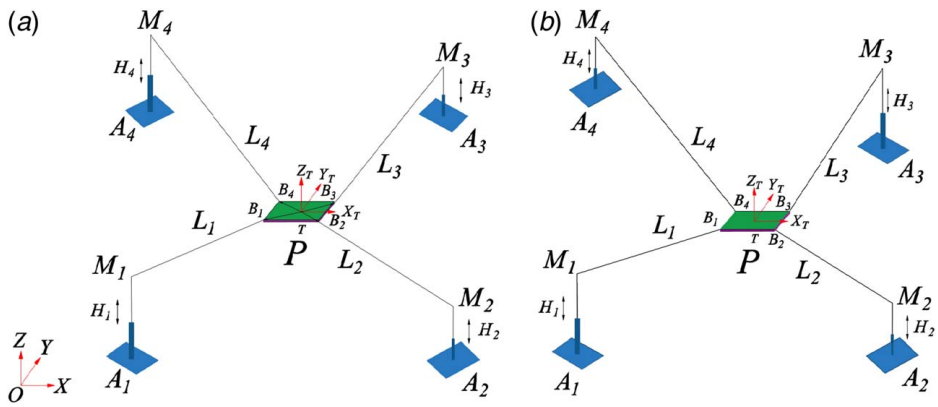

Fig. 2 Structural schematic of the CDPR: (*a*) Configuration 1, (*b*) Configuration 2

Zhang et al. [34] proposed two new indices, including actuation and constraint performance indices, and a performance evaluation and optimization design method of CDPRs was proposed based on the force transmission analysis. Hamida et al. [35] studied a suitable architecture with optimal dimensions by considering several optimality criteria and indices. A non-redundant CDPR for high-speed translational motion was designed with passive springs and parallel cables by Shao et al. [36], and an optimization method for high-speed CDPRs was proposed to optimize geometric parameters based on workspace and force transmission indices. The previous research studies mainly solve optimization problems by using existing optimization algorithms and proposing new optimization approaches. However, there are still some inadequacies in terms of optimization effects for optimization algorithms in the above work, and optimization indices and optimization design methods have little benefit for the optimization results of CDPRs.

To solve the above issues on the effectiveness of optimization algorithms applied in CDPRs, an adaptive adjustment inertia weight particle swarm optimization (AAIWPSO) algorithm is proposed in this paper based on a multi-objective optimization model. The purpose of the AAIWPSO algorithm is to improve the efficiency and accuracy of the particle swarm optimization (PSO) algorithm for solving the optimization problem of the designed CDPR, which can provide references for the improvement of other optimization algorithms for performance indices of CDPRs. Meanwhile, kinematic and static models of the CDPR for the large storage space are proposed in this paper. Two performance indices including workspace and dexterity are derived.

The remainder of this paper is organized as follows. Section 2 introduces the mechanical design and kinematic and static modeling of the CDPR. In Sec. 3, performance indices including workspace and dexterity are derived based on kinematic and static models. Section 4 establishes the multi-objective optimization model; subsequently, the AAIWPSO algorithm is proposed to solve the optimization results of performance indices. Section 5 gives some numerical examples to demonstrate convergence speed and solve the accuracy of the proposed AAIWPSO algorithm when compared with those of the PSO algorithm for the optimal design of CDPR with different configurations and masses of end-effectors. Meanwhile, optimization results obtained by the AAIWPSO algorithm and traditional genetic algorithm (GA) are compared. Some conclusions are summarized in Sec. 6.

2 Kinematic and Static Modeling of the CDPR

In this section, the mechanical design of the CDPR is introduced. Thus, the kinematic and static models are established.

2.1 Mechanical Design. In this paper, the mechanical model of the CDPR applied to large storage space is designed. The mechanical prototype and structural schematic are shown in Figs. 1 and 2, respectively. As shown in Fig. 1(*a*), the CDPR consists of four driving units, parallel cables, and a central mobile platform. Every driving unit is mainly divided into five parts: a cable reel, a reducer, an AC servo motor, a motor cabinet, and a shell of the driving unit. The central mobile platform consists of a workbench, pulley blocks, a lifting mechanism, an AC servo motor, a trimming motor, a charging box, and an end-effector. The end-effector consists of two guide bars, an electric screw, and a mechanical gripper.

As shown in Fig. 1(*a*), four driving units are symmetrically distributed in four directions of large storage space. The central mobile platform is respectively connected to four driving units through four cables. Every cable connects with a cable reel to realize the translational motion through a pulley block. These pulley blocks are fixed on the workbench, which can maintain the fast movement of the central mobile platform. A universal ball connecting with the lifting mechanism is installed in the workbench. Owing to the different heights of driving units, the pose of the end-effector can be adjusted accordingly. The lifting mechanism is driven by the AC servo motor under the central mobile platform. Noteworthily, the state of motion of the end-effector is consistent with that of the lifting mechanism in the Z-axis direction. The central mobile platform with three degrees-of-freedom can carry out arbitrary translational motion in space. The movement of the central mobile platform is controlled by pulling cables through driving units. When the central mobile station reaches a specified position, the end-effector can be lowered into the designated position by the lifting mechanism driven by the AC servo motor in the workbench.

As shown in Fig. 2, the structural schematic diagram was simplified based on the structural characteristics. The purpose of this is to facilitate theoretical analysis. Owing to the distance of a certain cable from the reel of the driving unit to the corresponding pulley block on the workbench is equal to the distance of the cable to the fixed end of the driving unit after bypassing the pulley block, the amplitude and direction of the force on the two ropes are the same in the meantime. Thus, a group of parallel cables is regarded as a cable. Noteworthily, the length of elongation or shortening of a cable is half the actual length of it. As shown in Fig. 2, two configurations of CDPR are given in this paper. As shown in Fig. 2(*a*), characteristics of Configurational 1 are $H_1 = H_4$, $H_2 = H_3$, $H_1(H_4) > H_2(H_3)$; as shown in Fig. 2(*b*), characteristics of Configurational 2 are $H_1 = H_3$, $H_2 = H_4$, $H_1(H_3) > H_2(H_4)$.

The mechanical structure of the mechanical gripper is shown in Fig. 3. The mechanical gripper is composed of a palm, cables, two cable reels, springs, a coupling, a servo motor, two driving motors, pulleys, knuckles, and fingers. Every knuckle is connected to a driving motor through a cable, and the driving motor is fixed to the palm. Every cable connects with a driving motor to realize the change of motion states of knuckles and fingers through pulleys. To keep the curved status of fingers in some positions, a flexible spring is located between the first and second knuckles of a finger. As shown in Figs. 1 and 3, when the end-effector reaches a designated position, the mechanical gripper is driven by an electric screw in the *X*-axis direction to

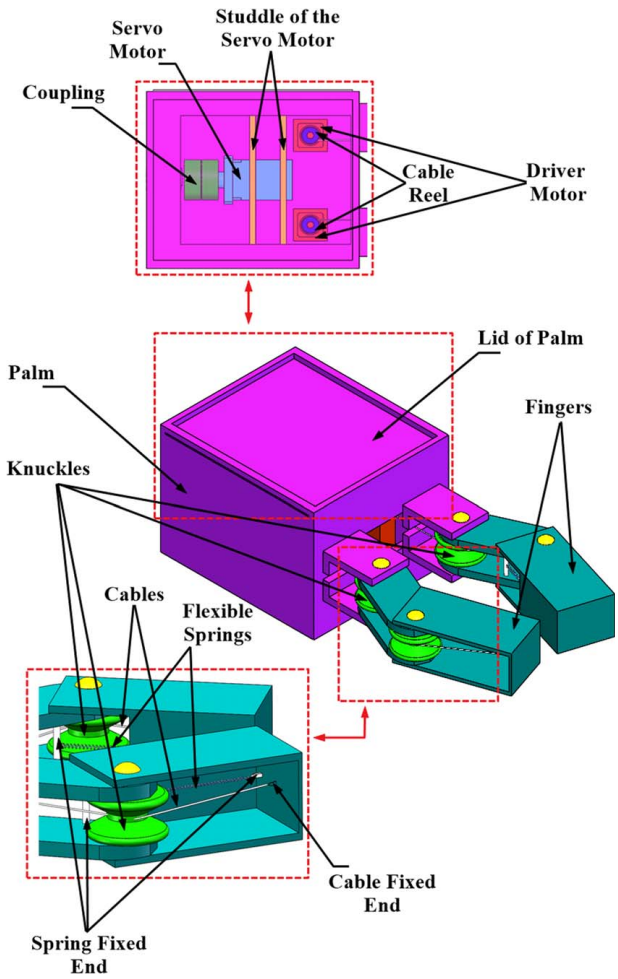

Fig. 3 Mechanical structure of the mechanical gripper

arrive at the vicinity of the grasped object. Subsequently, fingers are driven by pulling cables through driving motors inside the palm to grasp the object.

2.2 Kinematic Modeling. As shown in Fig. 2, A_i are intersection points between columns and the ground, M_i are attachment points of cables on the driving units, and B_i are attachment points of cables on the end-effector. A fixed cartesian frame $O-XYZ$ is attached to the base plane with its origin O at the center of the plane consisting of A_1, A_2, A_3, and A_4, and the X-axis is parallel to A_1A_2. A moving cartesian frame $T-X_TY_TZ_T$ is attached to the end-effector P with its origin T coinciding with the center of it, and the Y-axis is parallel to B_1B_4. Thus, the pose matrix of the moving frame relative to the fixed frame is expressed as

$$
{}^{O}_{T}\boldsymbol{R} = \boldsymbol{R}_Z(\alpha)\boldsymbol{R}_Y(\beta)\boldsymbol{R}_X(\gamma) = \begin{bmatrix} c\alpha & -s\alpha & 0 \\ s\alpha & c\alpha & 0 \\ 0 & 0 & 1 \end{bmatrix} \begin{bmatrix} c\beta & 0 & s\beta \\ 0 & 1 & 0 \\ -s\beta & 0 & c\beta \end{bmatrix} \times \begin{bmatrix} 1 & 0 & 0 \\ 0 & c\gamma & -s\gamma \\ 0 & s\gamma & c\gamma \end{bmatrix} \tag{1}
$$

$$
{}^{O}_{T}\boldsymbol{R} = \begin{bmatrix} c\alpha c\beta & c\alpha s\beta s\gamma - s\alpha c\gamma & c\alpha s\beta c\gamma + s\alpha s\gamma \\ s\alpha c\beta & s\alpha s\beta s\gamma + c\alpha c\gamma & s\alpha s\beta c\gamma - c\alpha s\gamma \\ -s\beta & c\beta s\gamma & c\beta c\gamma \end{bmatrix} \tag{2}
$$

where α, β, and γ are rotation angles of the moving frame around the Z-axis, Y-axis, and X-axis, respectively.

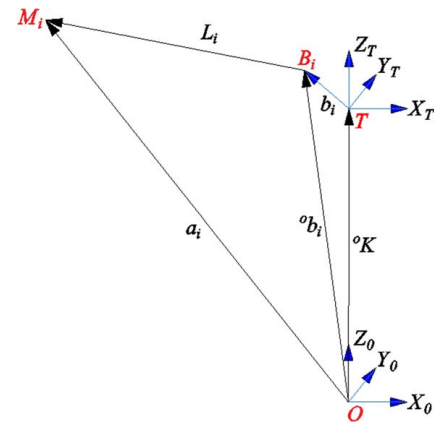

Fig. 4 Kinematic diagram

The kinematic diagram of the CDPR is shown in Fig. 4. Coordinates of M_i with respect to the fixed frame are denoted as $\boldsymbol{a}_i$ and coordinates of B_i with respect to the moving frame is denoted as $\boldsymbol{b}_i$ and

$$
\begin{aligned}
a_1 &= \begin{pmatrix} -\frac{f_1}{2} & -\frac{f_2}{2} & h \end{pmatrix}^T, \quad a_2 = \begin{pmatrix} \frac{f_1}{2} & -\frac{f_2}{2} & e \end{pmatrix} \\
a_3 &= \begin{pmatrix} \frac{f_1}{2} & \frac{f_2}{2} & e \end{pmatrix}^T, \quad a_4 = \begin{pmatrix} -\frac{f_1}{2} & \frac{f_2}{2} & h \end{pmatrix}^T
\end{aligned} \tag{3}
$$

$$
\begin{aligned}
b_1 &= \begin{pmatrix} -\frac{s_1}{2} & -\frac{s_2}{2} & \frac{s_3}{2} \end{pmatrix}^T, \quad b_2 = \begin{pmatrix} \frac{s_1}{2} & -\frac{s_2}{2} & -\frac{s_3}{2} \end{pmatrix}^T \\
b_3 &= \begin{pmatrix} \frac{s_1}{2} & \frac{s_2}{2} & -\frac{s_3}{2} \end{pmatrix}^T, \quad b_4 = \begin{pmatrix} -\frac{s_1}{2} & \frac{s_2}{2} & \frac{s_3}{2} \end{pmatrix}^T
\end{aligned} \tag{4}
$$

where f_2 are lengths of A_1A_4 and A_2A_3; f_1 are lengths of A_1A_2 and A_3A_4; h are heights of A_1M_1 and A_4M_4; e are heights of A_2M_2 and A_3M_3; s_2 are lengths of B_1B_4 and B_2B_3; s_1 are lengths of B_1B_2 and B_3B_4; and s_3 is the thickness of the end-effector.

The position vector ${}^{O}\boldsymbol{K}$ is set from O to T, and it can be expressed as ${}^{O}\boldsymbol{K} = (x\ y\ z)^T$. $\boldsymbol{a}_i$ and $\boldsymbol{b}_i$ are denoted as position vectors of $\boldsymbol{OM}_i$ and $\boldsymbol{TB}_i$, respectively. ${}^{O}\boldsymbol{b}_i$ is denoted as the position vector of $\boldsymbol{OB}_i$. Thus, the ith cable vector $\boldsymbol{L}_i$ can be obtained by

$$
\boldsymbol{L}_i = \boldsymbol{a}_i - {}^{O}\boldsymbol{b}_i = \boldsymbol{a}_i - {}^{O}\boldsymbol{K} - {}^{O}_{T}\boldsymbol{R}\boldsymbol{b}_i, \qquad i = 1,\ 2, \ldots,\ 4 \tag{5}
$$

The length of the ith cable l_i can be calculated by

$$
l_i = \|\boldsymbol{L}_i\| = \sqrt{\boldsymbol{L}_i^T \boldsymbol{L}_i} \tag{6}
$$

Taking the derivative of Eq. (6) with respect to time yields

$$
\dot{\boldsymbol{L}} = \boldsymbol{J}\dot{\boldsymbol{q}} \tag{7}
$$

where $\boldsymbol{J}$ is the Jacobian matrix of the CDPR; $\dot{\boldsymbol{q}}$ is the velocity vector of the end-effector; and

$$
\dot{\boldsymbol{L}} = \begin{pmatrix} \dot{l}_1 & \ldots & \dot{l}_4 \end{pmatrix}^T \tag{8}
$$

$$
\dot{\boldsymbol{q}} = \begin{pmatrix} \dot{x} & \dot{y} & \dot{z} \end{pmatrix}^T \tag{9}
$$

$$
\boldsymbol{J} = -\begin{pmatrix} \frac{\partial \boldsymbol{L}}{\partial x} & \frac{\partial \boldsymbol{L}}{\partial y} & \frac{\partial \boldsymbol{L}}{\partial z} \end{pmatrix} \tag{10}
$$

2.3 Static Modeling. The force analysis diagram of the CDPR is shown in Fig. 5. P is the center of the central mobile platform of the CDPR. To simplify the analysis, cables are assumed to be in tension and regarded as ideal straight lines without weight and

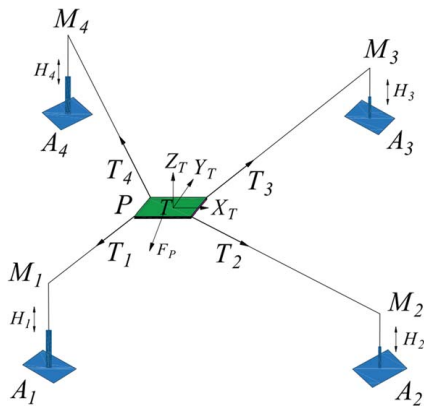

Fig. 5 Force analysis diagram of the CDPR

elasticity. According to the principle of moment balance, the static equation of the CDPR is expressed as

$$\begin{cases} \sum_{i=1}^{4} \boldsymbol{T}_i + \boldsymbol{F}_P = 0 \\ \sum_{i=1}^{4} \boldsymbol{b}_i \times \boldsymbol{T}_i + \boldsymbol{M}_Q = 0 \end{cases}, \quad i = 1, 2, \ldots, 4 \tag{11}$$

where $\boldsymbol{T}_i = T_i \boldsymbol{u}_i$ is the vector of tension of the ith cable; T_i is the scalar of tension of the ith cable; $\boldsymbol{u}_i = \boldsymbol{L}_i / l_i$ is the unit vector of the ith cable; $\boldsymbol{F}_P$ is the net force on the P; $\boldsymbol{b}_i$ is the vector of B_i in the moving cartesian frame; $\boldsymbol{M}_Q$ is the external torque on the P; $\boldsymbol{W} = \{\boldsymbol{F}_P^T, \ \boldsymbol{M}_Q^T\}^T$ is the wrench on the P. Thus, based on Eq. (11), one has

$$\begin{Bmatrix} \boldsymbol{u}_1 & \ldots & \boldsymbol{u}_n \\ \boldsymbol{b}_1 \times \boldsymbol{u}_1 & \ldots & \boldsymbol{b}_n \times \boldsymbol{u}_n \end{Bmatrix} \begin{Bmatrix} T_1 \\ \vdots \\ T_n \end{Bmatrix} = -\boldsymbol{W}, \qquad n = 4 \tag{12}$$

where $\boldsymbol{S}_i = \begin{Bmatrix} \boldsymbol{u}_i \\ \boldsymbol{b}_i \times \boldsymbol{u}_i \end{Bmatrix}$ is the linear vector of the ith cable. Thus, based on Eq. (12), one has

$$\boldsymbol{S} \cdot \boldsymbol{T} = -\boldsymbol{W} \tag{13}$$

where

$$\begin{cases} T = \{\boldsymbol{T}_1 \quad \ldots \quad \boldsymbol{T}_n\}^T \\ S = \{\boldsymbol{S}_1 \quad \ldots \quad \boldsymbol{S}_n\}^T \end{cases}, \ n = 4 \tag{14}$$

where $\boldsymbol{T}$ and $\boldsymbol{S}$ are vectors of tensions of cables and the structure matrix of the static model, respectively.

Based on Eqs. (12)–(14) and using the principle of virtual work yields

$$\boldsymbol{T}^T \cdot \Delta \boldsymbol{l} + \boldsymbol{W} \cdot \Delta \boldsymbol{x} = 0 \tag{15}$$

where

$$\begin{cases} \Delta l = \begin{pmatrix} l_1 & \ldots & l_n \end{pmatrix}^T \\ \Delta x = (\dot{x} \quad \dot{y} \quad \dot{z})^T \end{cases}, \ n = 4 \tag{16}$$

in which $\Delta \boldsymbol{l}$ and $\Delta \boldsymbol{x}$ are displacement increments of cables and the virtual displacement of the center P, respectively. Based on Eqs. (10), (13), and (15), the static model of the CDPR can be expressed as

$$\boldsymbol{J}^T \cdot \boldsymbol{T} = -\boldsymbol{W} \tag{17}$$

3 Performance Indices

In this section, based on kinematic and static models in Secs. 2.2 and 2.3, the performance indices including workspace and dexterity are derived.

3.1 Workspace. The workspace of the CDPR depends on the configuration of the mechanism, including the number of cables, the connection position between each cable and the static platform, and the connection position between each cable and the moving platform [37]. The workspace of the CDPR is divided into five categories, including the static equilibrium workspace, the wrench closure workspace, the wrench feasible workspace, the dynamic workspace, and the collision-free workspace. The static equilibrium workspace of the CDPR is discussed in this paper. It refers to the set of positions and poses of the CDPR that can keep still when only the gravity of the end-effector is considered [38]. Based on the above factors and kinematic modeling in Sec. 2, the workspace index for this CDPR can be expressed as

$$W_G = \frac{\int dV_Q}{V} = \frac{\iiint dxdydz}{V} \tag{18}$$

where W_G is the workspace index for the CDPR; V_Q is the actual workspace of the CDPR; V is the equivalent workspace (i.e., the circumscribed cuboid of the actual workspace). Thus, the efficiency of the workspace is directly proportional to W_G. Note that ranges of W_G change from 0 to 1 and W_G is a standardized index. Furthermore, the closer the workspace index W_G gets to 1, the larger the actual workspace is. If W_G is equal to 1, which means that the CDPR can move to any position in the task space.

3.2 Dexterity. For the central mobile platform of the CDPR, it can reach a certain working position under the pull of cables. Thus, the better the coordinated response performance of the end-effector at this working position, the more dexterous the CDPR is. Generally, dexterity is evaluated by the dexterous solid angle (the ratio of the volume of a reachable area to the volume of a sphere encircling the reachable area). However, this operation has to calculate redundant solutions for every working position. Thus, a quantitative analysis method is proposed for calculating dexterity [39]. For the CDPR, the reciprocal of the condition number of the Jacobian matrix is between 0 and 1; thus, the reciprocal of the condition number of the Jacobian matrix is regarded as an important dexterity index.

The dexterity of the CDPR refers to the transitivity of velocity and coordination of cables and end-effector. The Jacobian matrix can relate the velocity of the end-effector to the velocities of cables. Thus, the Jacobian equation is expressed in Eq. (7). Based on the structure description of the CDPR in Fig. 2, and Eqs. (7) and (8), the length vector of cables can be denoted as $\boldsymbol{L} = \begin{pmatrix} l_1 & \ldots & l_n \end{pmatrix}^T$, $n = 4$. Thus, the Jacobian matrix $\boldsymbol{J}$ can be expressed as

$$\boldsymbol{J} = -\begin{pmatrix} \boldsymbol{u}_i^T & ({}_T^O\boldsymbol{R}\boldsymbol{b}_i \times \boldsymbol{u}_i)^T \end{pmatrix} \tag{19}$$

Note that $\boldsymbol{J}$ is related to lengths of cables determined by the position of the end-effector, and the Jacobian matrix $\boldsymbol{J}$ is a 4×6 matrix. Thus, the pseudo-inverse matrix $\boldsymbol{J}^{-1}$ is regarded as the inverse matrix of $\boldsymbol{J}$. Subsequently, the unit velocity vector of the end-effector satisfies

$$\dot{\boldsymbol{q}}^T \cdot \dot{\boldsymbol{q}} = (\boldsymbol{J}^{-1}\dot{\boldsymbol{L}})^T \cdot (\boldsymbol{J}^{-1}\dot{\boldsymbol{L}}) = \dot{\boldsymbol{L}}^T (\boldsymbol{J}\boldsymbol{J}^T)^{-1} \dot{\boldsymbol{L}} = 1 \tag{20}$$

If $\boldsymbol{D}$ is denoted as $\boldsymbol{J}\boldsymbol{J}^T$, thus, Eq. (20) can be equivalently transformed to

$$\dot{\boldsymbol{L}}^T \boldsymbol{D}^{-1} \dot{\boldsymbol{L}} = 1 \tag{21}$$

Note that the matrices $\boldsymbol{D}$ and $\boldsymbol{D}^{-1}$ are symmetric positive-definite matrices. For any $\boldsymbol{D}^{-1}$, the velocity vector of cables $\dot{\boldsymbol{L}}$ satisfy the

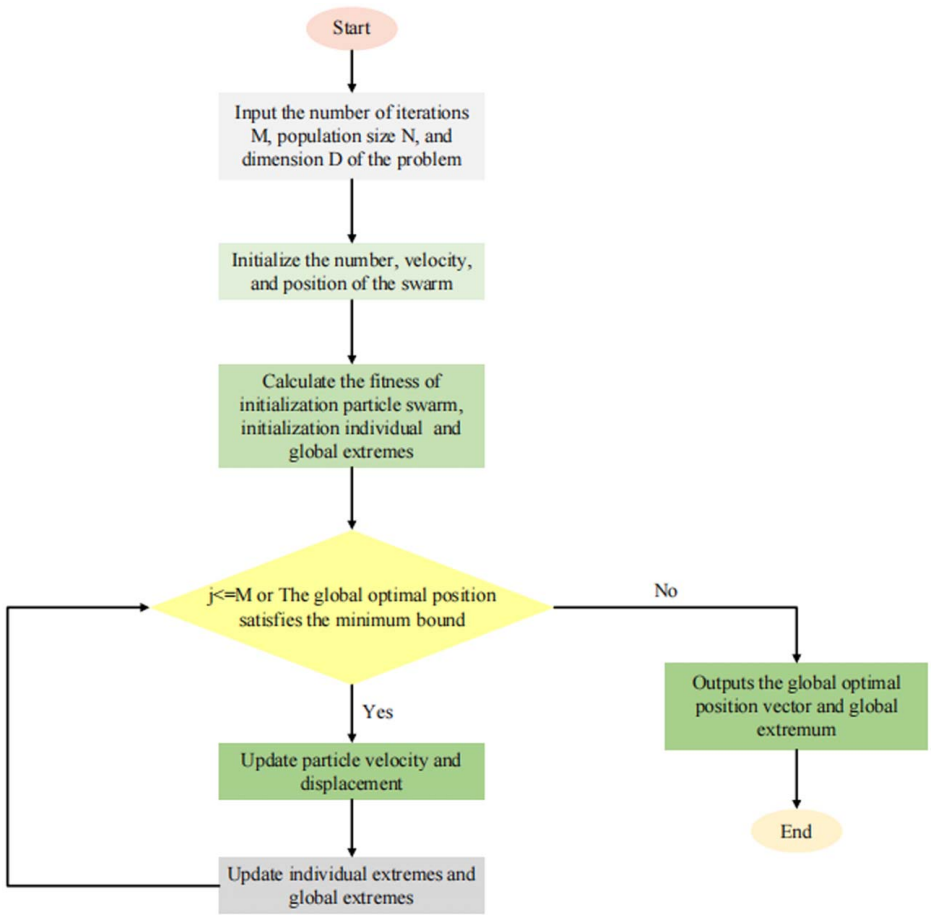

Fig. 6 Flowchart of the PSO algorithm

condition in Eq. (21). This proves that the matrix $\boldsymbol{D}$ can reflect the dexterity of the end-effector under the pull of cables. Thus, the condition number of the matrix $\boldsymbol{D}$ is qualified to measure the dexterity of the CDPR, and

$$m(\boldsymbol{D}) = \|\boldsymbol{D}\|_2 \cdot \|\boldsymbol{D}^{-1}\|_2 = \frac{\sigma_{\max}(\boldsymbol{D})}{\sigma_{\min}(\boldsymbol{D})} \geq 1 \tag{22}$$

where $\|\boldsymbol{D}\|_2$ represents the 2-norm of the matrix $\boldsymbol{D}$; $\sigma_{\max}(\boldsymbol{D})$ and $\sigma_{\min}(\boldsymbol{D})$ are the maximal and minimal eigenvalues of the matrix $\boldsymbol{D}$. In this paper, c is defined as the reciprocal of the condition number of $\boldsymbol{J}$, and

$$c = \frac{1}{m(\boldsymbol{D})} \tag{23}$$

The index c can measure the ability to move along every axis in a certain configuration state. Owing to the Jacobian matrix being determined by the configuration of the CDPR, c is a local index for the dexterity of the CDPR. Subsequently, it is necessary to evaluate the global dexterity index for the CDPR. The global dexterity index is defined as the integral of the local dexterity index over the reachable workspace [39]. Thus, the global dexterity index is expressed as

$$\eta = \frac{\int_{E_0}^{E_n} c \, dE}{\int_{E_0}^{E_n} dE} \tag{24}$$

where E_0 and E_n denote the first and last points of the whole workspace, respectively.

As a whole, η, between 0 and 1, is a global dexterity index of the CDPR. Note that the closer the index η to 1, the better dexterous of the CDPR is, which means that the CDPR is fully isotropic. Obviously, when the index η approaches to 0, the poorer the dexterous of the CDPR is, which means that the CDPR is located in a singular state.

4 Multi-Objective Optimal Design

In this section, a multi-objective optimization model is established. Subsequently, by introducing an adaptive adjustment inertia weight to the PSO algorithm, the AAIWPSO algorithm is proposed.

4.1 Multi-Objective Optimization Model. The workspace and dexterity indices are two important performance characteristics for the multi-objective optimal design of the CDPR. Generally, there are common methods to transform multi-objective optimization problems to single objective optimization problems. The multi-objective multiplication and division method [40] of the optimal theory is adopted in this paper. Thus, a multi-objective optimization model of the CDPR is established by the product of W_G and η, which can be defined as follows:

$$\begin{cases} \max \quad K = W_G(d) \cdot \eta\,(d) \\ s.t. \quad d_{i_{\min}} < d_i < d_{i_{\max}} \qquad i = 1, \ldots, n \end{cases} \tag{25}$$

where $d = (d_1, \ldots, d_i, \ldots, d_n)$ is the set of constraint functions; n is the total number of constraint functions; W_G is the workspace index for the CDPR given in Eq. (18); and η is the global dexterity index given in Eq. (24). In this optimization process, the set of constraint functions includes m and H_i, which represent the mass of the end-effector and heights of driving units, respectively, as shown

in Fig. 2. In this paper, the value range of m is 6 kg $< m <$ 20 kg, and the value range of H_i ($i = 1, 2, 3, 4$) is 2 $m < H_i < 5$ m.

4.2 Particle Swarm Optimization Algorithm. The basic idea of the PSO algorithm is to find the optimal solution based on the cooperation and information sharing between individuals in a group. The flowchart of the PSO algorithm is shown in Fig. 6, and particles need to update positions and velocities after determining individual and global extremes, and the iterative equation is given as follows:

$$\begin{cases} v_{jD}^{M+1} = wv_{jD}^{M} + c_1 r_1 (p_{jD}^{M} - t_{jD}^{M}) + c_2 r_2 (b_{jD}^{M} - t_{jD}^{M}) \\ t_{jD}^{M+1} = t_{jD}^{M+1} + t_{jD}^{M+1} \end{cases} \tag{26}$$

where M is the number of iterations; c_1 and c_2 are learning factors of the algorithm; r_1 and r_2 are random numbers in the range of [0, 1]; w is the inertia weight; D is the dimension of the problem; v_j is the set of velocity of the jth particle, and $v_j = v_{j_1}, \ldots, v_{j_D}$, $j = 1, 2, \ldots, D$; j is the subscript of the jth particle; p_j and b_j are sets of individual and global extremes of the optimal position for current iteration number, respectively, and $p_j = p_{j_1}, \ldots, p_{j_D}$, $b_j = b_{j_1}, \ldots, b_{j_D}$, $j = 1, 2, \ldots, D$; and t_j is the set of the position of the jth particle, $t_j = t_{j_1}, \ldots, t_{j_D}$, $j = 1, 2, \ldots, D$.

To locate the optimal values of W_G and η for the CDPR, the PSO algorithm is used to deal with the optimization problem. As shown in Fig. 6, based on the flowchart of the PSO algorithm, the optimization process is summarized as follows:

(1) Compile the PSO algorithm in MATLAB according to the objective function and constraints.
(2) Set initial parameters for the PSO algorithm: fitness function (the fitness function equals the objective function in this paper) K, position coordinates of the end-effector x, $y \in (-2500, 2500)$ and $z \in (0, 5000)$, particle population size $N = 10$, the maximum number of iterations $M = 300$, inertia weight $w = 0.8$, and learning factors $c_1 = c_2 = 2$.
(3) Run the program. Optimal results for the CDPR with Configurations 1 and 2 are listed in Table 6. From Table 6, one finds that, for Configuration 1 with masses of the end-effector being 6 kg and 20 kg, the optimization results by the PSO algorithms can achieve $W_G = 0.6241$, $\eta = 0.5065$, $K = 0.3162$, and $W_G = 0.2125$, $\eta = 0.2042$, $K = 0.0434$, respectively; for Configuration 2, the optimization results by the PSO algorithms can achieve $W_G = 0.7049$, $\eta = 0.5457$, $K = 0.3847$, and $W_G = 0.3369$, $\eta = 0.2119$, $K = 0.0714$, respectively.

4.3 AAIWPSO Algorithm. The PSO algorithm can avoid crossover and mutation operations and has been applied in performance index optimization with a fast search speed. Furthermore, owing to the simple iterative process and few tuning parameters, the PSO algorithm can be directly applied to engineering implementation. However, due to the lack of dynamic adjustment of search speed, the PSO algorithm is prone to the state of local optimal. Therefore, the convergence accuracy of the PSO algorithm is usually low. Note that an inertia weight w can be described as the effect of the previous velocity of a particle on current velocity. The capability of local and global optimization of the PSO algorithm is decided by the size of the inertia weight w. Generally, the range of w is 0–1. As w is close to 0, the capability of local optimization of the PSO algorithm is stronger; as w is close to 1, the capability of global optimization of the PSO algorithm is stronger.

To gain better optimization results of performance indices of the CDPR, an AAIWPSO algorithm is proposed based on the PSO algorithm and the multi-objective optimization model, and the inertia equation of the inertia weight w is expressed as

$$w = \begin{cases} w_{\max} - (w_{\max} - w_{\min}) \cdot \dfrac{f(x_{jn}^N) - f_{\min}^N}{f_{av}^N - f_{\min}^N}, & f(x_{jn}^N) \le f_{av}^N \\ w_{\min}, & f(x_{jn}^N) > f_{av}^N \end{cases} \tag{27}$$

where $w_{\min}$ and $w_{\max}$ are the maximum and minimum coefficients of inertia weigh, respectively; $f_{\min}^N$ is the minimum fitness of all particles with Nth iteration, and $f_{\min}^N = \min\{f(x_{j_1}^N), f(x_{j_2}^N), f(x_{j_3}^N), \ldots, f(x_{j_n}^N)\}$; f_{av}^N is the average fitness of all particles with Nth iteration; $f(x_{jn}^N)$ is the fitness value of current particle with Nth iteration. Similarly, the equation of the position and velocity of the particles is expressed in Eq. (26). As shown in Eq. (27), the updating mode of w is nonlinear. The value of w varies with the change in the fitness value of the particle. When $f(x_{jn}^N)$ approaches the local optimal value, the value of w increases; otherwise, it decreases. When $f(x_{jn}^N) > f_{av}^N$, the value of $w = w_{\min}$ is small, which protects the current particle; when $f(x_{jn}^N) \le f_{av}^N$. The value of w calculated based on Eq. (27) is large, which allows the particle to move towards a better search area.

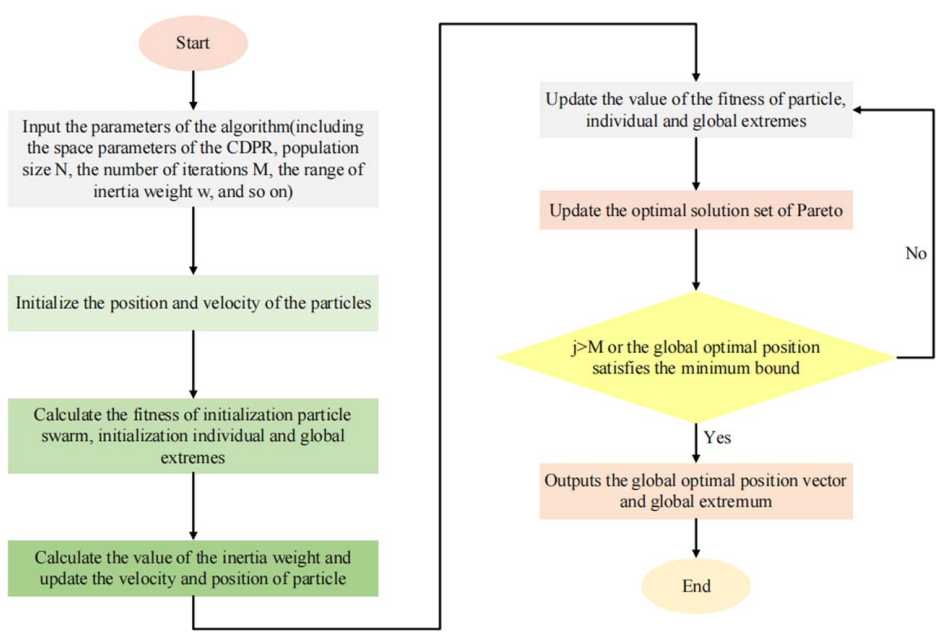

Fig. 7 Flowchart of the AAIWPSO algorithm

The flowchart of the AAIWPSO algorithm is shown in Fig. 7, and the optimization process is summarized as follows:

(1) Compile the PSO algorithm in MATLAB according to the objective function and constraints.
(2) Set initial parameters for the AAIWPSO algorithm: fitness function K, position coordinates of the end-effector x, $y \in (-2500, 2500)$ and $z \in (0, 5000)$, particle population size $N = 10$, the maximum number of iterations $M = 300$, inertia weight $w \in (0.4, 0.9)$, and learning factors $c_1 = c_2 = 2$.
(3) Run the program. Optimal results for the CDPR with Configurations 1 and 2 are listed in Table 6. From Table 6, one finds that, for Configuration 1 with masses of the end-effector being 6 kg and 20 kg, the optimization results by the AAIWPSO algorithm can achieve $W_G = 0.6731$, $\eta = 0.5672$, $K = 0.3818$, and $W_G = 0.2269$, $\eta = 0.2195$, $K = 0.0498$, respectively; for Configuration 2, the optimization results by the AAIWPSO algorithm can achieve $W_G = 0.7689$, $\eta = 0.5927$, $K = 0.4558$, and $W_G = 0.3632$, $\eta = 0.2244$, $K = 0.0815$, respectively.

For a solution of the optimization problem in this paper, if no other solutions can dominate the solution, then the solution is called a Pareto optimal solution [41]. The set of all optimal solutions is called the optimal solution set of Pareto. In this paper, the dense distance method is used to update the optimal solution set of Pareto. Meanwhile, the updated formula is shown in Eq. (28). The update method is as follows:

(1) Judge whether the number of solutions exceeds the upper limit (in this paper, the upper limit of the set is 300) in the optimal solution set of Pareto. If not, the current optimal solution is added to the set; otherwise, one proceeds to the next step.
(2) Calculate the dense distance between the two closest solutions to the current optimal solution in the optimal solution set of Pareto based on Eq. (28).
(3) Compare two dense distances calculated in step two; the solution with a smaller dense distance is eliminated. Meanwhile, the current optimal solution is added to the optimal set.

The density distance is calculated as follows:

$$I(x_i) = \frac{|W_G(x_j) - W_G(x_k)|}{W_{G\max}} + \frac{|\eta(x_j) - \eta(x_k)|}{\eta_{\max}} \tag{28}$$

where x_j and x_k are the two closest particles to x_i; $W_G(x_j)$ is the value of W_G for particle x_j; $W_G(x_k)$ is the value of W_G for particle x_k; $\eta(x_j)$ is the value of η for particle x_j; $\eta(x_k)$ is the value of η for particle x_k; and $W_{G\max}$ and $\eta_{\max}$ are the maximum for W_G and η, respectively.

5 Numerical Examples

In this section, some numerical examples on kinematics, workspace, and dexterity of the CDPR are given, and optimization results based on PSO and AAIWPSO algorithms are compared and analyzed.

The trajectory generation of the CDPR is important to explore the change in the length of each cable in the process of motion. Common trajectories include the spiral trajectory, the sine trajectory, and so on [42]. As shown in Fig. 8, assuming the trajectory of the end-effector in space is a spiral and the equation of the trajectory of the end-effector is expressed as

$$\begin{cases} x = R(t) \cdot \cos(\omega t) \\ y = R(t) \cdot \sin(\omega t) \\ z = vt_a + \frac{1}{2} a t_a^2 \\ R(t) = z \cdot \tan \varepsilon + r \end{cases} \tag{29}$$

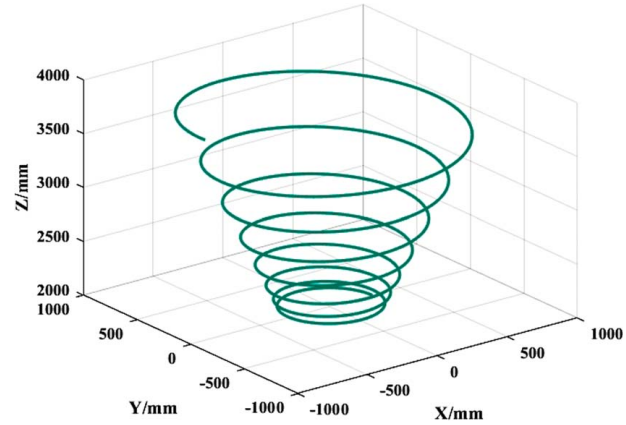

Fig. 8 Spiral trajectory of end-effector

where r is the radius of conical trajectory in the space; ω is the angular velocity of end-effector; t is a certain point in a period of time; $v = 2$ is the velocity of the end-effector; a is the acceleration of the end-effector; ε is the conical angle of spiral trajectory; t_a is the total time of motion. Values of system parameters are listed in Table 1.

5.1 Effects of Different Configurations and Masses of End-Effectors on the Workspace of the CDPR. The workspace of the CDPR is analyzed based on the Monte Carlo simulation (MCS) method, and the control variable method is used to calculate the size of the workspace in different cases. In this paper, the workspace is equivalent to the static workspace that denotes the set of all end-effector positions satisfying the following relation:

$$\{\boldsymbol{Q}: rank(\boldsymbol{S}) = 3 \cap (T_{\min} < T_i < T_{\max})\} \tag{30}$$

where $T_{\max}$ and $T_{\min}$ are maximum and minimum tensions of cables, respectively; $\boldsymbol{Q}$ is the workspace of the CDPR.

Three-dimensional point cloud of the workspace is constructed according to the MCS method. Assuming that $N = 50000$, $T_{\max} = 200\ N$, $T_{\min} = 0$ $x \in (-x_0, x_0)$, $y \in (-y_0, y_0)$, and $z \in (0, H_0)$. The flowchart of the MCS for calculating the workspace of the CDPR is shown in Fig. 9, and the algorithm for obtaining optimal workspace distribution of the CDPR is listed in Table 2.

The volume of the workspace is not visually represented. Thus, the calculation equation of the workspace is expressed as

$$V_Q = \frac{N'}{N}(|X_{\max} - X_{\min}| \cdot |Y_{\max} - Y_{\min}| \cdot |Z_{\max} - Z_{\min}|) \tag{31}$$

where $X_{\max}$ and $X_{\min}$ are maximum and minimum values of the X-axis for the workspace of the CDPR, respectively; $Y_{\max}$ and $Y_{\min}$ are maximum and minimum values of the Y-axis for the workspace of the CDPR, respectively; $Z_{\max}$ and $Z_{\min}$ are maximum and minimum values of the Z-axis for the workspace of the CDPR, respectively; N' is the number of points that satisfies the constraint in Eq. (30). Note that two key factors for calculating the size of the workspace are heights of driving units H_i and the weight of the end-effector m.

Table 1 Main parameters of the end-effector

Symbols	Descriptions	Values
r(mm)	Initial radius	300
ω(rad/s)	Angular velocity of end-effector	$\pi/2$
t(s)	Certain time	[0, 30]
v(mm/s)	Velocity of end-effector	2
a(mm/s^2)	Acceleration of end-effector	4
ε(deg)	Conical angle of end-effector	60
t_a(s)	Total time	30

The effects of heights of driving units on the workspace of the CDPR are shown in Fig. 10. The mass of the end-effector is 6 kg, and angles between projections of adjacent driving units on the same plane are $\theta_1 = \theta_2 = \theta_3 = \theta_4 = 90$ deg. Owing to the limitation of the size of the whole space, the length, and width of driving units are limited to 5 m, and the height is limited to between 2 m and 5 m. Figure 10 shows that the volume of the workspace of the CDPR decreases with the vertical distance between the low and high driving units decreasing in a certain configuration. Note that the volume and shape of the workspace of the CDPR with Configuration 2 are different from those of the CDPR with Configuration 1. Volumes of the workspace of the CDPR with Configurations 1 and 2 are listed in Table 3. From Table 3, it can be concluded that when the heights of low and high driving units of the CDPR with Configuration 1 are the same as those of the CDPR with Configuration 2, the volume of the workspace of the CDPR with Configuration 2 is larger than those of the CDPR with Configuration 1. It is also concluded that the larger the distance between low and high driving units, the larger the volume of the workspace.

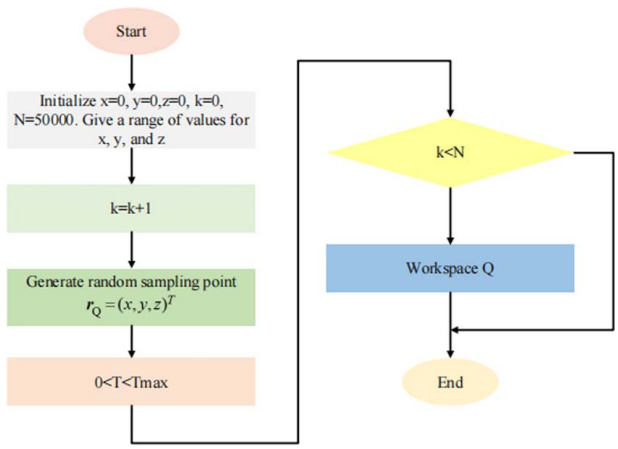

Fig. 9 Flowchart of the MCS for calculating the workspace of the CDPR

Effects of masses of end-effectors on the workspace of the CDPR are shown in Fig. 11. The range of the mass of the end-effector m changes from 6 kg to 20 kg, angles between projections of adjacent driving units on the same plane are $\theta_1 = \theta_2 = \theta_3 = \theta_4 = 90$ deg, heights of driving units are $H_1 = H_4 = 5$ m and $H_2 = H_3 = 2$ m. Figure 11 shows that the volume of the workspace of the CDPR decreases with the increase in the mass of the end-effector in a certain configuration. Note that the shape of the workspace of the CDPR remains unchanged in a certain configuration. Volumes of the workspace of the CDPR with Configurations 1 and 2 are listed in Table 4. From Fig. 11 and Table 4, it can be concluded that the mass of the end-effector has a significant impact on the volume of the workspace, and the volume of the workspace becomes less with the increase of the mass of the end-effector. Note that the volume of the workspace of the CDPR with Configuration 2 is larger than those with Configuration 1 with the same mass as the end-effector.

5.2 Effects of Different Configurations and Masses of End-Effectors on the Dexterity of the CDPR. For two configurations of the CDPR, the local dexterity index c in Eq. (25) for all reachable points can be calculated. Effects of different configurations and masses of end-effectors on the dexterity of the CDPR are shown in Fig. 12. The figure shows that distributions of dexterity of the CDPR with different masses of end-effectors in Configurations 1 and 2 nearly are almost consistent, and values of local dexterity of the CDPR with Configuration 2 are higher than those of the CDPR with Configuration 1. Note that the closer positions of the end-effector to high driving units, larger values of local dexterity, and the closer positions of the end-effector to the center of the workspace with a three-dimensional point cloud of the CDPR, larger values of local dexterity.

Values of global dexterity of the CDPR with Configurations 1 and 2 with different masses of end-effectors are listed in

Table 2 Algorithm for obtaining optimal workspace distribution of the CDPR

Algorithm 1: Optimal Workspace Distribution of the CDPR

Input: pose matrix, Jacobi matrix, and statics equation of the CDPR ${}^{O}_{T}\boldsymbol{R} \in \mathbb{R}^n$, and $\boldsymbol{J} \in \mathbb{R}^n$, the minimum and maximum cable tension matrix of the CDPR $\boldsymbol{T}_{min} \in \mathbb{R}^m$, and $\boldsymbol{T}_{max} \in \mathbb{R}^m$ (m = n + 1), sampling range of x, y, z $x \in (-2500, 2500)$, $y \in (-2500, 2500)$, and $z \in (0, 5000)$, the end-effector mass m, the driving the unit position matrix $\boldsymbol{a}$, the workbench vertex matrix $\boldsymbol{b}$, a random number with a limited range com (the limited range in this work is $0 < com < T_{max}$).

Output: the workspace with three-dimensional point cloud of the CDPR $\boldsymbol{Q}$

Initialize $\boldsymbol{Q} = \{\boldsymbol{s}_1, \boldsymbol{s}_2, \boldsymbol{s}_3\}$;
$\boldsymbol{R} \leftarrow$ Position matrix ${}^{O}_{T}\boldsymbol{R}$
$\boldsymbol{J} \leftarrow$ Jacobian matrix $\boldsymbol{J}$
$\boldsymbol{s}_1, \boldsymbol{s}_2, \boldsymbol{s}_3 \leftarrow$ Null array
for $k \leftarrow 1$ to N **do**
  $\{x = -2500 + rand \cdot 5000,\ y = -2500 + rand \cdot 5000,\ z = 2000 + rand \cdot 3000\}$
  $\{\boldsymbol{L}_i = -\boldsymbol{J} - \boldsymbol{R} \cdot \boldsymbol{b} + \boldsymbol{a},\quad i = 1, \ldots, 4\}$
  $\{l_i = sqrt(\boldsymbol{L}_i \cdot \boldsymbol{L}_i),\quad i = 1, \ldots, 4\}$
  $\left\{\boldsymbol{u}_i = \dfrac{\boldsymbol{L}_i}{l_i},\quad i = 1, \ldots, 4\right\}$
  $\boldsymbol{A} \leftarrow$ Unit matrix of cables length $\boldsymbol{u}_i$
  $\boldsymbol{w} = [0; 0; k]$
  $r \leftarrow rank(\boldsymbol{A})$
  if $r == 3$ then
    $\boldsymbol{q} = \boldsymbol{A} \backslash \boldsymbol{w}$
    $\boldsymbol{Ot} \leftarrow$ Orthonormal basis for the null space of $\boldsymbol{A}$
    for $com \leftarrow 0$ to T_{max} **do**
      if $(\boldsymbol{q} + com \cdot \boldsymbol{Ot}) \leq \boldsymbol{T}_{max}$ && $q + com \cdot \boldsymbol{Ot} > \boldsymbol{T}_{min}$ **then**
        $\{\boldsymbol{s}_1(i) = x,\ \boldsymbol{s}_2(i) = y,\ \boldsymbol{s}_3(i) = z\}$
      end
    end
  end
  $\boldsymbol{Q} \leftarrow$ point that satisfies conditions in the spatial coordinate system
end
return $\boldsymbol{Q}$

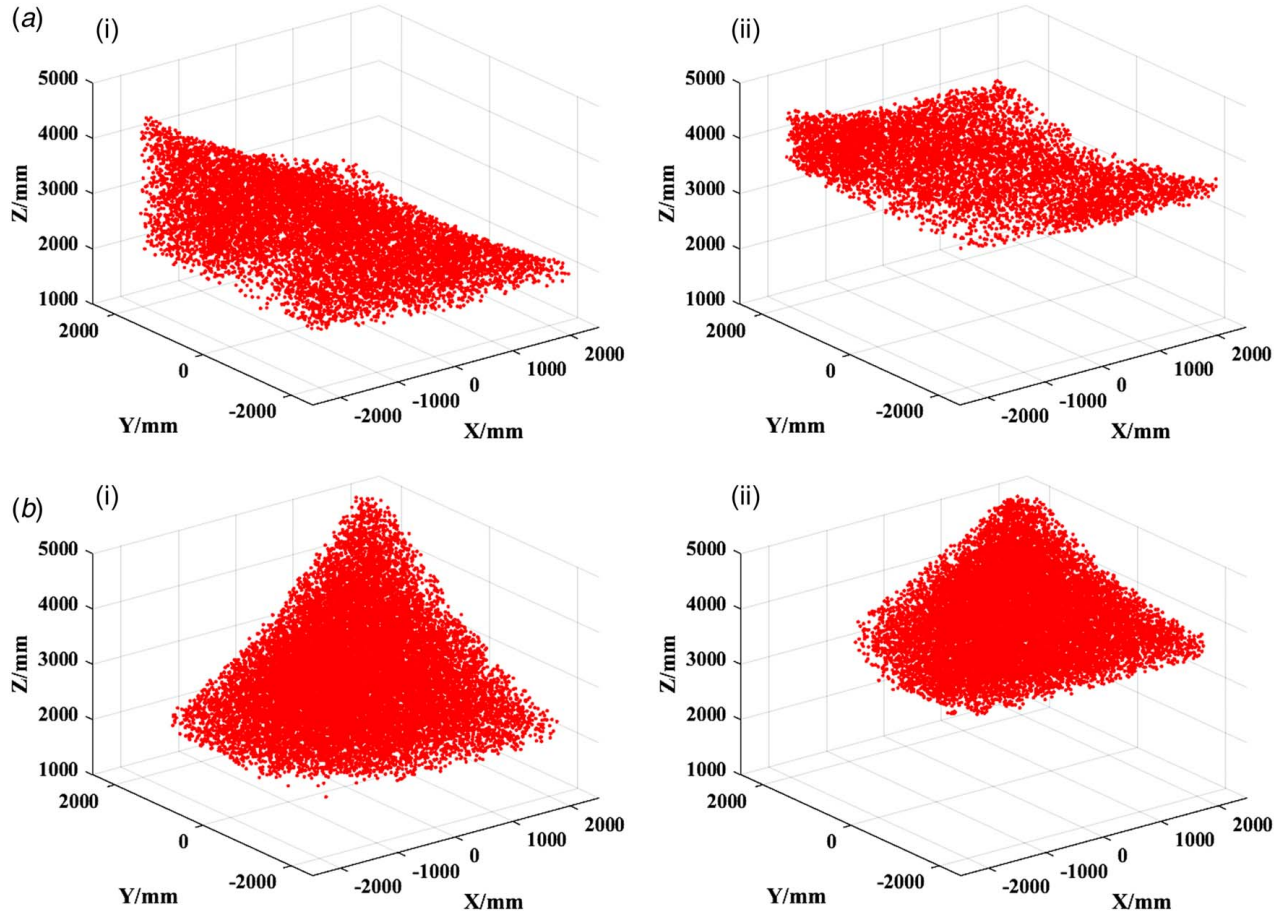

Fig. 10 Workspace of the CDPR with Configurations 1 and 2 with different heights of driving units: (*a*) Configuration 1, (i) $H_1 = H_4 = 5$ m, $H_2 = H_3 = 2$ m, (ii) $H_1 = H_4 = 5$ m, $H_2 = H_3 = 3.5$ m, and (*b*) Configuration 2. (i) $H_1 = H_3 = 5$ m, $H_2 = H_4 = 2$ m (ii) $H_1 = H_3 = 5$ m, $H_2 = H_4 = 3.5$ m

Table 3 Volumes of the workspace of the CDPR with Configurations 1 and 2 with different heights of driving units

Configurations	Heights of driving units	Volumes of workspace (m^3)	Structural schematics
Configuration 1	$H_1 = H_4 = 5$ m $H_2 = H_3 = 2$ m	27.392	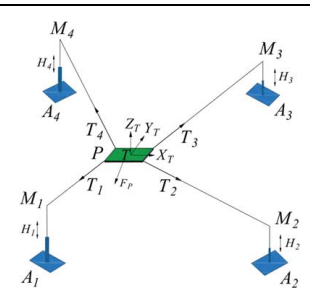
	$H_1 = H_4 = 5$ m $H_2 = H_3 = 3.5$ m	11.237	
Configuration 2	$H_1 = H_3 = 5$ m $H_2 = H_4 = 2$ m	31.164	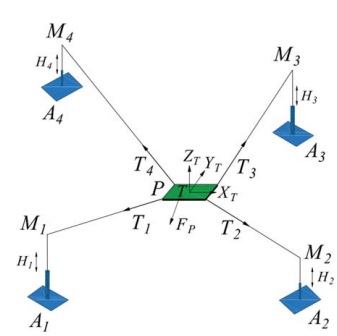
	$H_1 = H_3 = 5$ m $H_2 = H_4 = 3.5$ m	16.571	

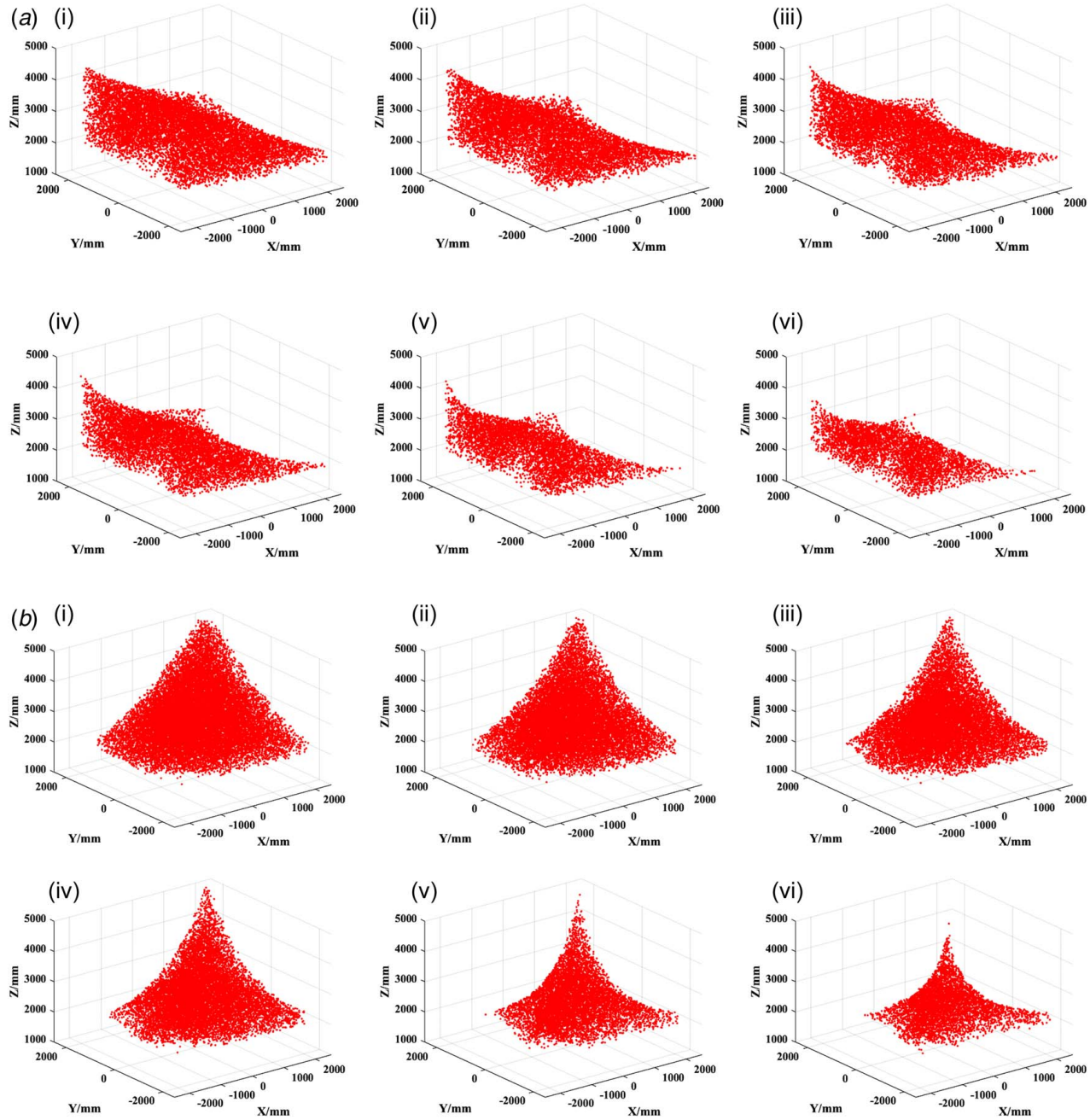

Fig. 11 Workspace of the CDPR with configurations 1 and 2 with different masses of end-effectors: (*a*) Configuration 1, (i) $m = 6$ kg, (ii) $m = 10$ kg, and (iii) $m = 12$ kg, (iv) $m = 14$ kg, (v) $m = 18$ kg, and (vi) $m = 20$ kg, and (*b*) Configuration 2, (i) $m = 6$ kg, (ii) $m = 10$ kg, and (iii) $m = 12$ kg, (iv) $m = 14$ kg, (v) $m = 18$ kg, and (vi) $m = 20$ kg

Table 5. From Table 5, it can be concluded that the value of the global dexterity of the CDPR decreases with the increase in the mass of the end-effector in a certain configuration. Note that the value of global dexterity of the CDPR with Configuration 2 is larger than those with Configuration 1 with the same mass of the end-effector.

5.3 Comparison Analysis Between the AAIWPSO Algorithm, Particle Swarm Optimization Algorithm, and Genetic Algorithm. AAIWPSO algorithm, PSO algorithm, and GA are used to solve optimal results of the multi-objective optimization model of the CDPR. Comparisons of three optimization algorithms for the CDPR with Configurations 1 and 2 are shown in Fig. 13. The figure shows that values of fitness function (objective function) for the CDPR with Configurations 1 and 2 by the AAIWPSO algorithm are higher than those by the PSO algorithm and GA. As shown in Fig. 13(*a*), in Configuration 1, numbers of iteration by AAIWPSO algorithm, PSO algorithm, and GA are 33, 57, and 65, respectively; In Configuration 2, numbers of iteration by AAIWPSO algorithm, PSO algorithm, and GA are 43, 85, and 144, respectively. As shown in Fig. 13(*c*), in Configuration 1, numbers of iteration by AAIWPSO algorithm, PSO algorithm, and GA are 101, 175, and 118, respectively; In Configuration 2, numbers of iteration by AAIWPSO algorithm, PSO algorithm, and GA are 162, 189, and 172 respectively. The above results show that the AAIWPSO algorithm can achieve a much higher convergence speed than PSO algorithm and GA. At the same time, owing to the randomness of the inertia weight w in Eq. (27) in the AAIWPSO algorithm, the possibility of falling into local optimal values by the AAIWPSO

Table 4 Volumes of the workspace of the CDPR with Configurations 1 and 2 with different masses of end-effectors

Configurations	m (kg)	Heights of driving units (m)	Volumes of workspace (m^3)	W_G
Configuration 1	6	$H_1 = H_4 = 5$	27.392	0.6848
	10	$H_2 = H_3 = 2$	23.292	0.5823
	12		21.184	0.5296
	14		18.092	0.4523
	18		12.056	0.3014
	20		9.188	0.2297
Configuration 2	6	$H_1 = H_3 = 5$	31.164	0.7791
	10	$H_2 = H_4 = 2$	27.136	0.6784
	12		25.26	0.6315
	14		23.932	0.5983
	18		18.988	0.4747
	20		14.564	0.3641

Table 5 Values of the global dexterity of the CDPR with Configurations 1 and 2 with different masses of end-effectors

Configurations	m (kg)	Heights of driving units (m)	Values of global dexterity, η
Configuration 1	6	$H_1 = H_4 = 5$	0.5881
	10	$H_2 = H_3 = 2$	0.4891
	12		0.4311
	14		0.4155
	18		0.2631
	20		0.2215
Configuration 2	6	$H_1 = H_3 = 5$	0.6213
	10	$H_2 = H_4 = 2$	0.5827
	12		0.5326
	14		0.4793
	18		0.3684
	20		0.2356

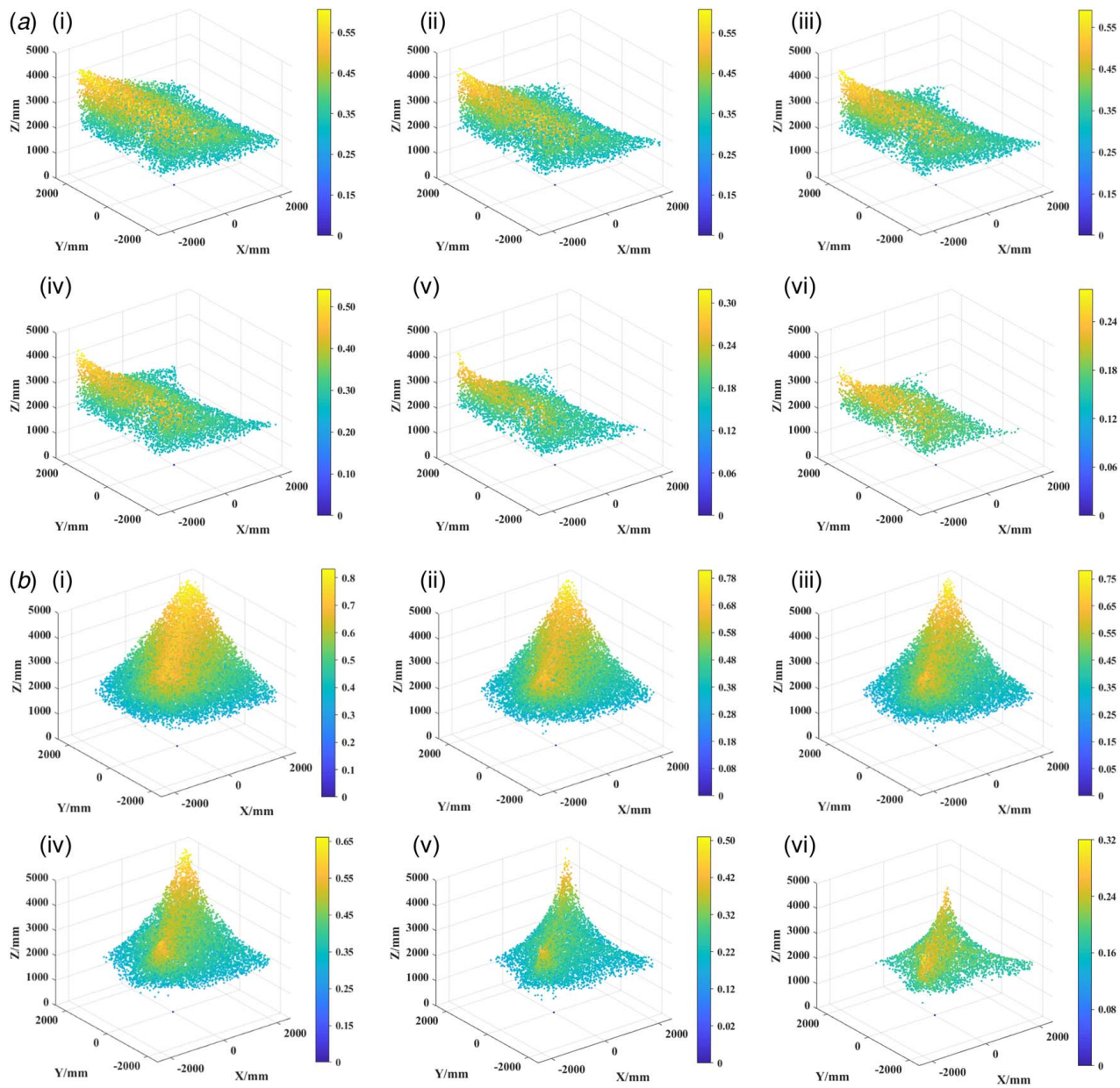

Fig. 12 Dexterity of the CDPR with different configurations and masses of end-effectors: (*a*) Configuration 1, (i) $m = 6$ kg, (ii) $m = 10$ kg, and (iii) $m = 12$ kg, (iv) $m = 14$ kg, (v) $m = 18$ kg, and (vi) $m = 20$ kg and (*b*) Configuration 2, (i) $m = 6$ kg, (ii) $m = 10$ kg, and (iii) $m = 12$ kg, (iv) $m = 14$ kg, (v) $m = 18$ kg, and (vi) $m = 20$ kg

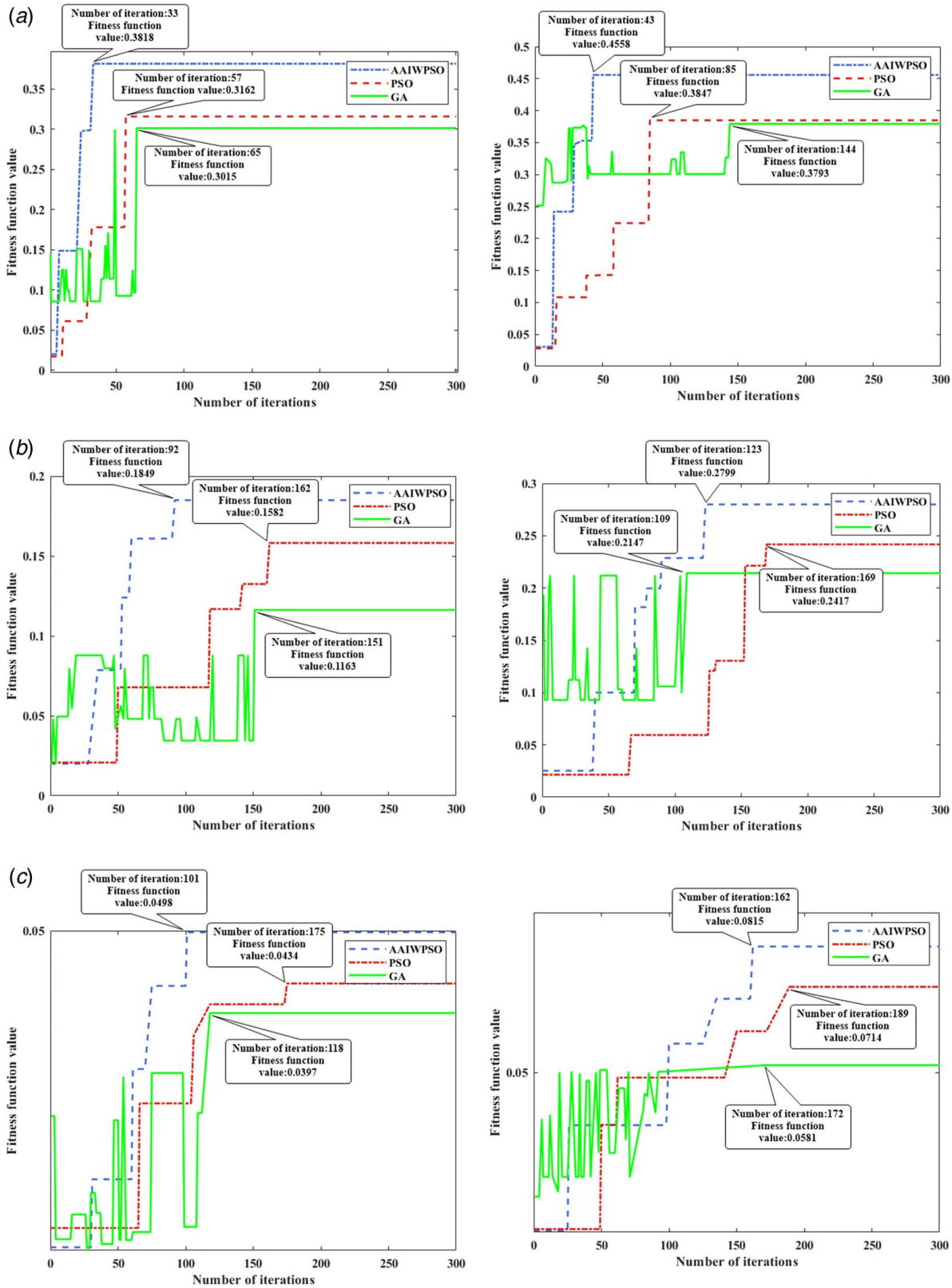

Fig. 13 Comparisons of three optimization algorithms for Configurations 1 and 2: (*a*) $m = 6$ kg, (*b*) $m = 14$ kg, and (*c*) $m = 20$ kg

algorithm is lower than that by the PSO algorithm. Thus, the solution accuracy obtained by the AAIWPSO algorithm is higher than that obtained by the PSO algorithm. Meanwhile, the convergence stability and solution accuracy of the AAIWPSO algorithm is better than that of GA in the optimization process.

Optimal results of AAIWPSO algorithm, PSO algorithm, and GA for the CDPR with Configurations 1 and 2 are listed in Table 6. For Configuration 1 with masses of end-effectors being 6 kg and 20 kg, the optimization results by the AAIWPSO algorithm, PSO algorithm, and GA can achieve $W_G = 0.6731$, $\eta = 0.5672$, $K =$

Table 6 Optimal results of the AAIWPSO algorithm, PSO algorithm, and GA for the CDPR with Configurations 1 and 2

		AAIWPSO algorithm			PSO algorithm			GA		
Configurations	m	K	W_G	η	K	W_G	η	K	W_G	η
1	6	0.3818	0.6731	0.5672	0.3162	0.6241	0.5065	0.3015	0.6268	0.4810
2		0.4558	0.7689	0.5927	0.3847	0.7049	0.5457	0.3793	0.6784	0.5591
1	10	0.2741	0.5755	0.4763	0.2316	0.5381	0.4304	0.2068	0.5172	0.3998
2		0.3822	0.6742	0.5669	0.3269	0.6347	0.5150	0.2915	0.6031	0.4833
1	12	0.2246	0.5236	0.4290	0.1913	0.4823	0.3966	0.1702	0.4369	0.3896
2		0.3271	0.6275	0.5213	0.2803	0.5814	0.4821	0.2642	0.5521	0.4785
1	14	0.1849	0.4485	0.4123	0.1582	0.4131	0.3829	0.1163	0.3562	0.3302
2		0.2799	0.5922	0.4726	0.2417	0.5358	0.4511	0.2142	0.5117	0.4186
1	18	0.0784	0.2921	0.2620	0.0673	0.2682	0.2509	0.0589	0.2447	0.2407
2		0.1685	0.4713	0.3575	0.1468	0.4371	0.3358	0.1175	0.3899	0.3013
1	20	0.0498	0.2269	0.2195	0.0434	0.2125	0.2042	0.0397	0.2013	0.1972
2		0.0815	0.3632	0.2244	0.0714	0.3369	0.2119	0.0581	0.2764	0.2102

0.3818; $W_G = 0.6241$, $\eta = 0.5065$, $K = 0.3162$, and $W_G = 0.6268$, $\eta = 0.4810$, $K = 0.3015$; $W_G = 0.2269$, $\eta = 0.2195$, $K = 0.0498$, $W_G = 0.2125$, $\eta = 0.2042$, $K = 0.0434$, and $W_G = 0.2013$, $\eta = 0.1972$, $K = 0.0397$, respectively; for Configuration 2 with the masses of end-effectors being 6 kg and 20 kg, the optimization results by the AAIWPSO algorithm, PSO algorithm, and GA can achieve $W_G = 0.7689$, $\eta = 0.5927$, $K = 0.4558$, $W_G = 0.7049$, $\eta = 0.5457$, $K = 0.3847$, and $W_G = 0.6784$, $\eta = 0.5591$, $K = 0.3793$; $W_G = 0.3632$, $\eta = 0.2244$, $K = 0.0815$, $W_G = 0.3369$, $\eta = 0.2119$, $K = 0.0714$, and $W_G = 0.2764$, $\eta = 0.2102$, $K = 0.0581$, respectively.

The above results show that values of W_G, η, and K by the AAIWPSO algorithm are almost 7.85%, 11.98%, and 20.75% higher than those by the PSO algorithm for the CDPR with the optimal design of Configuration 1, respectively; values of W_G, η, and K by the AAIWPSO algorithm are almost 9.08%, 8.61%, and 18.48% higher than those by the PSO algorithm for the CDPR with the optimal design of Configuration 2, respectively. Meanwhile, values of W_G, η, and K by the AAIWPSO algorithm are almost 7.38%, 17.92%, and 26.63% higher than those by the GA for the CDPR with the optimal design of Configuration 1, respectively; values of W_G, η, and K by the AAIWPSO algorithm are almost 13.34%, 6.01%, and 20.17% higher than those by the GA for the CDPR with the optimal design of Configuration 2, respectively.

The above results also show that values of objective function K by the AAIWPSO algorithm are almost 14∼20% and 19∼40% higher than those by the PSO algorithm and GA with masses of end-effectors being 6–20 kg. The optimization effects including convergence efficiency and accuracy by the traditional PSO algorithm and GA are much lower than those by AAIWPSO algorithm. Comparing the optimal results obtained by the optimization of the three algorithms with the real calculation results, the optimization results of AAIWPSO algorithm are much closer to the real results listed in Tables 4 and 5. Meanwhile, the end-effector mass is larger, the closer the optimization results by the AAIWPSO algorithm are to real values.

6 Conclusion

In this paper, an AAIWPSO algorithm based on the PSO algorithm is presented for the optimization of performance indices of CDPR. In particular, two performance indices are proposed to prove and evaluate the optimal solution. A novel CDPR mechanism with two non-adjacent driving units constituting a diagonal configuration is designed. The kinematic model of CDPR is established based on the inverse kinematic analysis, and the static model of CDPR is established according to force and external torque analysis of statics. Thus, two performance indices including workspace and dexterity are derived. The ranges of two performance indices are limited to 0∼1 to obtain quantitative results. Subsequently, the multi-objective optimization model including objective function and constraints is established. The AAIWPSO algorithm introduces an adaptive adjustment inertia weight to improve the convergence efficiency and accuracy of the traditional PSO algorithm. PSO algorithm, GA, and AAIWPSO algorithm are respectively used to optimize the objective function. Numerical examples demonstrate that the AAIWPSO algorithm can achieve a much higher convergence speed and lower possibility of falling into local optimal solutions than the PSO algorithm. In addition, the convergence stability of AAIWPSO algorithm is better than that of GA in the optimization process. Besides, values of the objective function for the CDPR by the AAIWPSO algorithm are almost 14–20% and 19–40% higher than those by the PSO algorithm and GA with different configurations and masses of end-effectors.

Acknowledgment

This work was supported by the National Natural Science Foundation of China (Grant Nos. 52205258 and 51925502) and the Anhui Provincial Natural Science Foundation (Grant No. 2108085QE218).

Conflict of Interest

There are no conflicts of interest.

Data Availability Statement

The authors attest that all data for this study are included in the paper.

Nomenclature

a = acceleration of the end-effector
c = reciprocal of the condition number of $\boldsymbol{J}$
d = set of constraint functions
e = height of A_2M_2 or A_3M_3
h = height of A_1M_1 or A_4M_4
j = subscript of the jth particle
m = mass of end-effector
r = radius of conical trajectory in the space
t = certain point in a period of time
v = velocity of the end-effector
w = inertia weight

D = dimension of the problem
K = multi-objective model
M = number of iterations
N = particle population size
P = end-effector
V = equivalent workspace
$\boldsymbol{D} = \boldsymbol{D} = \boldsymbol{J}\boldsymbol{J}^T$
$\boldsymbol{J}$ = Jacobian matrix
$\boldsymbol{Q}$ = workspace of CDPR
$\boldsymbol{S}$ = structure matrix of the static model
$\boldsymbol{T}$ = vectors of tensions of cables
$\boldsymbol{W}$ = external spanner on P
$\dot{\boldsymbol{q}}$ = velocity vector of the end-effector
N' = number of points those satisfy the constraint
${}^{O}\boldsymbol{K}$ = position vector
$\dot{\boldsymbol{L}}$ = velocity vector of cables
b_j = sets of global extremes of the optimal position for the current iteration number
c_1 = learning factor of the algorithm
c_2 = learning factor of the algorithm
f_1 = length of A_1A_2 or A_3A_4
f_2 = length of A_1A_4 or A_2A_3
l_i = length of the ith cable
p_j = sets of individuals of the optimal position for the current iteration number
r_1 = random number in the range of [0, 1]
r_2 = random number in the range of [0, 1]
s_1 = length of B_1B_2 or B_3B_4
s_2 = length of B_1B_4 or B_2B_3
s_3 = thickness of P
t_a = total time of motion
t_j = set of the position of the jth particle
v_j = set of the velocity of the jth particle
$w_{\max}$ = maximum coefficient of inertia weigh
$w_{\min}$ = minimum coefficient of inertia weigh
$\boldsymbol{a}_i$ = coordinates of M_i with respect to the fixed frame
$\boldsymbol{b}_i$ = coordinates of B_i with respect to the moving frame
$\boldsymbol{u}_i$ = unit vector of the ith cable
A_i = intersection points between columns and the ground
B_i = attachment points of cables on P
E_0 = first point of the whole reachable workspace
E_n = last point of the whole reachable workspace
H_i = height of ith driving unit
M_i = attachment points of cables on the driving units
$T_{\max}$ = maximum tension of cables
$T_{\min}$ = minimum tension of cables
V_Q = reachable workspace
$\boldsymbol{F}_P$ = net force on the P
$\boldsymbol{L}_i$ = ith cable vector
$\boldsymbol{M}_Q$ = external torque on P
$\boldsymbol{S}_i$ = linear vector of the ith cable
$\boldsymbol{T}_i$ = vector of tension of the ith cable
W_G = workspace index
f_{av}^N = average fitness of all particles with Nth iteration
$f_{\min}^N$ = minimum fitness of all particles with Nth iteration
${}^{O}\boldsymbol{b}_i$ = position vector of $\boldsymbol{OB}_i$
${}^{O}_{T}\boldsymbol{R}$ = pose matrix of the moving frame relative to the fixed frame
$E_0 \sim E_n$ = All reachable positions
$O-XYZ$ = fixed cartesian frame
$T-X_TY_TZ_T$ = moving cartesian frame
α = rotation angle of the moving frame around the Z-axis
β = rotation angle of the moving frame around the Y-axis
$\Delta\boldsymbol{l}$ = displacement increments of cables
$\Delta\boldsymbol{x}$ = virtual displacement of the end-effector
ε = conical angle of the spiral trajectory
γ = rotation angle of the moving frame around the X-axis
η = global dexterity index
θ_i = angles between projections of adjacent driving units on the same plane
ω = angular velocity of the end-effector

References

[1] Zhang, Z. K., Shao, Z. F., You, Z., Tang, X. Q., Zi, B., Yang, G. L., Gosslin, C., and Caro, S., 2022, "State-of-the-Art on Theories and Applications of Cable-Driven Parallel Robots," Front. Mech. Eng., **17**(3), p. 37.
[2] Zhang, B., Shang, W. W., Cong, S., and Li, Z. J., 2020, "Coordinated Dynamic Control in the Task Space for Redundantly Actuated Cable-Driven Parallel Robots," IEEE/ASME Trans. Mechatron., **26**(5), pp. 2396–2407.
[3] Sancak, C., and Itik, M., 2021, "Out-of-Plane Vibration Suppression and Position Control of a Planar Cable-Driven Robot," IEEE/ASME Trans. Mechatron., **27**(3), pp. 1311–1320.
[4] Paez-Granados, D. F., Kadone, H., Hassan, M., Chen, Y., and Suzuki, K., 2022, "Personal Mobility With Synchronous Trunk–Knee Passive Exoskeleton: Optimizing Human–Robot Energy Transfer," IEEE/ASME Trans. Mechatron., **27**(5), pp. 3613–3623.
[5] Duan, J. H., Shao, Z. F., Zhang, Z. K., and Peng, F. Z., 2022, "Performance Simulation and Energetic Analysis of TBot High-Speed Cable-Driven Parallel Robot," ASME J. Mech. Rob., **14**(2), p. 024504.
[6] Carbonari, L., Callegari, M., Palmieri, G., and Palpacelli, M. C., 2014, "Analysis of Kinematics and Reconfigurability of a Spherical Parallel Manipulator," IEEE Trans. Robot., **30**(6), pp. 1541–1547.
[7] Cuvillon, L., Weber, X., and Gangloff, J., 2020, "Modal Control for Active Vibration Damping of Cable-Driven Parallel Robots," ASME J. Mech. Rob., **12**(5), p. 051004.
[8] Hussein, H., Santos, J. C., and Gouttefarde, M., 2018, "Geometric Optimization of a Large Scale CDPR Operating on a Building Façade," Proceedings of the 2018 IEEE/RSJ International Conference on Intelligent Robots and Systems (IROS), Madrid, Spain, Oct. 1–5, pp. 5117–5124.
[9] Wang, Y. X., and Xu, Q. S., 2021, "Design and Testing of a Soft Parallel Robot Based on Pneumatic Artificial Muscles for Wrist Rehabilitation," Sci. Rep., **11**(1), p. 1273.
[10] Mamidi, T. K., and Bandyopadhyay, S., 2021, "Forward Dynamic Analyses of Cable-Driven Parallel Robots With Constant Input With Applications to Their Kinetostatic Problems," Mech. Mach. Theory, **163**, p. 104381.
[11] Fabritius, M., Martin, C., and Pott, A., 2018, "Calculation of the Collision-Free Printing Workspace for Fully-Constrained Cable-Driven Parallel Robots," Proceedings of the ASME 2018 International Design Engineering Technical Conferences and Computers and Information in Engineering Conference, Quebec City, Canada, Aug. 26–29, p. 51814, V05BT07A046.
[12] Liu, H. T., Huang, T., Chetwynd, D. G., and Kecskemethy, A., 2017, "Stiffness Modeling of Parallel Mechanisms at Limb and Joint/Link Levels," IEEE Trans. Robot., **33**(3), pp. 734–741.
[13] Jiang, Q. M., and Gosselin, C. M., 2008, "Singularity Equations of Gough–Stewart Platforms Using a Minimal Set of Geometric Parameters," ASME J. Mech. Des., **130**(11), p. 112303.
[14] Gao, C. Q., Huang, H. L., Li, Y., and Bing, L., 2022, "Design and Analysis of a Three-Fingered Deployable Metamorphic Robotic Grasper," ASME J. Mech. Des., **144**(8), p. 083302.
[15] Wu, C., Liu, X. J., Wang, L. P., and Wang, J. S., 2010, "Optimal Design of Spherical 5R Parallel Manipulators Considering the Motion/Force Transmissibility," ASME J. Mech. Des., **132**(3), p. 031002.
[16] Gao, H. B., Sun, G. Y., Liu, Z., Sun, C., Li, N., Ding, L., Yu, H. T., and Deng, Z. Q., 2022, "Tension Distribution Algorithm Based on Graphics With High Computational Efficiency and Robust Optimization for Two-Redundant Cable-Driven Parallel Robots," Mech. Mach. Theory, **172**, p. 104739.
[17] Zhang, W. X., Zhang, W., Ding, X. L., and Sun, L., 2020, "Optimization of the Rotational Asymmetric Parallel Mechanism for Hip Rehabilitation With Force Transmission Factors," ASME J. Mech. Rob., **12**(4), p. 041006.
[18] Gueners, D., Chanal, H., and Bouzgarrou, B. C., 2020, "Stiffness Optimization of a Cable Driven Parallel Robot for Additive Manufacturing," 2020 IEEE International Conference on Robotics and Automation (ICRA), Paris, France, May 31–Aug. 31, IEEE, pp. 843–849.
[19] Sun, C., Gao, H. B., Liu, Z., Xiang, S., Yu, H. T., Li, N., and Deng, Z. Q., 2021, "Design and Optimization of Three-Degree-of-Freedom Planar Adaptive Cable-Driven Parallel Robots Using the Cable Wrapping Phenomenon," Mech. Mach. Theory, **166**, p. 104475.
[20] Brahmi, B., Ahmed, T., Elbojairami, I. E., Swapnil, A. A. Z., Zaman, M. A. U., Schultz, K., McGonigle, E., and Rahman, M. H., 2021, "Flatness Based Control of a Novel Smart Exoskeleton Robot," IEEE/ASME Trans. Mechatron., **27**(2), pp. 974–984.
[21] Zhang, Z. K., Shao, Z. F., and Wang, L. P., 2020, "Optimization and Implementation of a High-Speed 3-DOFs Translational Cable-Driven Parallel Robot," Mech. Mach. Theory, **145**, p. 103693.
[22] Song, C., and Lau, D. W., 2022, "Workspace-Based Model Predictive Control for Cable-Driven Robots," IEEE Trans. Robot., **38**(4), pp. 2577–2596.
[23] Jamshidifar, H., Khajepour, A., and Korayem, A. H., 2021, "Wrench Feasibility and Workspace Expansion of Planar Cable-Driven Parallel Robots

by a Novel Passive Counterbalancing Mechanism," IEEE Trans. Robot., **37**(3), pp. 935–947.

[24] Gao, J., Zhou, B., Zi, B., Qian, S., and Zhao, P., 2022, "Kinematic Uncertainty Analysis of a Cable-Driven Parallel Robot Based on an Error Transfer Model," ASME J. Mech. Rob., **14**(5), p. 051008.

[25] Viegas, C., Daney, D., Tavakoli, M., and Almeida, A. T., 2017, "Performance Analysis and Design of Parallel Kinematic Machines Using Interval Analysis," Mech. Mach. Theory, **115**, pp. 218–236.

[26] Zhou, B., Zi, B., and Qian, S., 2017, "Dynamics-Based Nonsingular Interval Model and Luffing Angular Response Field Analysis of the DACS With Narrowly Bounded Uncertainty," Nonlinear Dyn., **90**(4), pp. 2599–2626.

[27] Zhang, X. B., Lu, Z. Z., and Cheng, K., 2021, "Reliability Index Function Approximation Based on Adaptive Double-Loop Kriging for Reliability-Based Design Optimization," Reliab. Eng. Syst. Saf., **216**, p. 108020.

[28] Wang, Z. L., Zhao, D. Y., and Guan, Y., 2023, "Flexible-Constrained Time-Variant Hybrid Reliability-Based Design Optimization," Struct. Multidiscipl. Optim., **66**(4), pp. 1–14.

[29] Yang, C., Ye, W., and Li, Q. C., 2022, "Review of the Performance Optimization of Parallel Manipulators," Mech. Mach. Theory, **170**, p. 104725.

[30] Chen, Y., Yan, J. Y., Feng, J., and Sareh, P., 2021, "Particle Swarm Optimization-Based Metaheuristic Design Generation of Non-Trivial Flat-Foldable Origami Tessellations With Degree-4 Vertices," ASME J. Mech. Des., **143**(1), p. 011703.

[31] Chu, S., Xiao, M., Gao, L., Zhang, Y., and Zhang, J. H., 2021, "Robust Topology Optimization for Fiber-Reinforced Composite Structures Under Loading Uncertainty," Comput. Methods Appl. Mech. Eng., **384**, p. 113935.

[32] Zhou, Q., Guo, S. J., Xu, L., Gao, X. X., Williams, H., Xu, H. M., and Yan, F. W., 2021, "Global Optimization of the Hydraulic-Electromagnetic Energy-Harvesting Shock Absorber for Road Vehicles With Human-Knowledge-Integrated Particle Swarm Optimization Scheme," IEEE/ASME Trans. Mechatron., **26**(3), pp. 1225–1235.

[33] Meng, Q. Z., Xie, F. G., Liu, X. J., and Takeda, Y. K., 2020, "Screw Theory-Based Motion/Force Transmissibility Analysis of High-Speed Parallel Robots With Articulated Platforms," ASME J. Mech. Rob., **12**(4), p. 041011.

[34] Zhang, D., and Wei, B., 2017, "Modelling and Optimisation of a 4-DOF Hybrid Robotic Manipulator," Int. J. Comput. Integr. Manuf., **30**(11), pp. 1179–1189.

[35] Hamida, I. B., Laribi, M. A., Mlika, A., Loft, R., Zeghloul, S., and Carbone, G., 2021, "Multi-Objective Optimal Design of a Cable Driven Parallel Robot for Rehabilitation Tasks," Mech. Mach. Theory, **156**, p. 104141.

[36] Zhang, Z. K., Shao, Z. F., Peng, F. Z., Li, H. S., and Wang, L. P., 2020, "Workspace Analysis and Optimal Design of a Translational Cable-Driven Parallel Robot With Passive Springs," ASME J. Mech. Rob., **12**(5), p. 051005.

[37] Hu, B., 2016, "Kinematically Identical Manipulators for the Exechon Parallel Manipulator and Their Comparison Study," Mech. Mach. Theory, **103**, pp. 117–137.

[38] Martin-Parra, A., Juarez-Perez, S., Gonzalez-Rodriguez, A., Gonzalez-Rodriguez, A. G., Lopez-Diaz, A. I., and Rubio-Gomez, G., 2023, "A Novel Design for Fully Constrained Planar Cable-Driven Parallel Robots to Increase Their Wrench-Feasible Workspace," Mech. Mach. Theory, **180**, p. 105159.

[39] Wang, J., and Lau, H. Y. K., 2021, "Dexterity Analysis Based on Jacobian and Performance Optimization for Multi-Segment Continuum Robots," ASME J. Mech. Rob., **13**(6), p. 061012.

[40] Brauers, W. K. M., and Zavadskas, E. K., 2012, "Robustness of MULTIMOORA: A Method for Multi-Objective Optimization," Informatica, **23**(1), pp. 1–25.

[41] Xiong, H., Cao, H. H., Zeng, W. F., Huang, J. C., Diao, X. M., Lu, W. J., and Lou, Y. J., 2022, "Real-Time Reconfiguration Planning for the Dynamic Control of Reconfigurable Cable-Driven Parallel Robots," ASME J. Mech. Rob., **14**(6), p. 060913.

[42] Syamlan, A. T., Nurahmi, L., Tamara, M. N., and Pramujati, B., 2020, "Dynamic Trajectory Planning of Reconfigurable Suspended Cable Robot," Int. J. Dyn. Control, **8**, pp. 887–897.